# Efficient Photovoltaic Current Generation at Ferroelectric Domain Walls

Jan Seidel,[1,2] Deyi Fu,[3,4] Seung-Yeul Yang,[3] Esther Alarcón-Lladó,[1,5] Junqiao Wu,[1,3] Ramamoorthy Ramesh,[1,2,3] and Joel W. Ager III[1,*]

[1]*Materials Sciences Division, Lawrence Berkeley National Laboratory, Berkeley, California, USA*
[2]*Department of Physics, University of California at Berkeley, Berkeley, California, USA*
[3]*Department of Materials Science and Engineering, University of California at Berkeley, Berkeley, California, USA*
[4]*School of Electronic Science and Engineering, Nanjing University, Nanjing, China*
[5]*Swiss Federal Institute of Technology (EPFL), Lausanne, Switzerland*

(Received 18 May 2011; revised manuscript received 2 July 2011; published 15 September 2011)

We elucidate the mechanism of a newly observed photovoltaic effect which occurs in ferroelectrics with periodic domain structures. Under sufficiently strong illumination, domain walls function as nanoscale generators of the photovoltaic current. The steps in the electrostatic potential function to accumulate electrons and holes on opposite sides of the walls while locally reducing the concentration of the oppositely charged carriers. As a result, the recombination rate adjacent to the walls is reduced, leading to a net diffusion current. In open circuit, photovoltages for periodically ordered domain walls are additive and voltages much larger than the band gap can be generated. The internal quantum efficiency for individual domain walls can be surprisingly high, approaching 10% for above band-gap photons. Although we have found the effect in $BiFeO_3$ films, it should occur in any system with a similar periodic potential.

DOI: 10.1103/PhysRevLett.107.126805 PACS numbers: 73.50.Pz, 77.80.Dj, 77.84.−s, 85.50.−n

Recently it was reported that large, above-band gap, photovoltages are generated by certain types of domain walls in thin films of multiferroic $BiFeO_3$ (BFO) [1]. Here, we elucidate the fundamental origin of this effect by considering the drift and diffusion dynamics of photogenerated carriers. The origin of the photovoltaic (PV) effect is electron-hole separation at ferroelectric domain walls; this process can be very efficient with internal quantum efficiencies exceeding 10% for above-band-gap light.

The requirements for the photovoltaic conversion of light to energy are (1) mobile charge carriers of opposite signs (e.g. electrons and holes), (2) splitting of the quasi-Fermi levels for these charge carriers under illumination, and (3) an asymmetry such that the contacts are carrier-selective [2]. In this context, the electric fields in ferroelectric (FE) materials have been of interest for providing the necessary asymmetry. Indeed, there is extensive literature describing FE photovoltaic effects [3–5]. One class of FE PV effects is attributed to asymmetric potentials around impurity atoms; these systems show below band gap response [6,7]. Above band gap voltages in polycrystalline FE materials have been attributed to series addition of the fields in different grains, as in a tandem solar cell [8]. Additive photovoltages have been also observed in polycrystalline semiconductors [9].

A major limitation in the understanding of these FE PV effects is incomplete knowledge of the nature of the electric fields proposed to produce the effect. This limitation does not apply to ferroelectric BFO. We have shown that BFO can satisfy the PV criteria listed above, using Schottky contacts to provide the transport asymmetry [10]. Moreover, thin films of BFO can be made with a periodic FE domain structure extending over 100's of microns [see Fig. 1(a)]. Thus in contrast to prior FE PV work, we know the location and magnitude of the built-in fields as illustrated in Fig. 1(b), which allows for a full microscopic understanding.

When BFO is grown epitaxially on insulating $DyScO_3$ by chemical vapor deposition, it spontaneously forms well-aligned 71° and/or 109° stripe FE domain structures [11]. The distance between the walls can be controlled between 50 and 300 nm by varying the film thickness.

Here we used 71° and 109° wall samples where the in-plane polarization component varies in a zig-zag pattern showing a defined net polarization direction across the film. Pt contacts with a separation between 20 to 200 $\mu$m parallel to the domain walls were deposited on

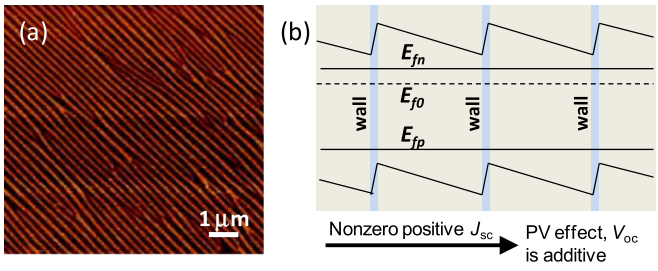


FIG. 1 (color online). (a) Piezoresponse force microscopy (PFM) image showing well-aligned arrays of 71° domain walls in BFO (b) Schematic of short-circuit band alignment and current flow under illumination (only 3 periods are shown). Split quasi-Fermi levels $E_{fn}$ and $E_{fp}$ for nonequilibrium electrons and holes are indicated. Wall width is exaggerated for clarity.

 

top of the thin film samples, as shown in Fig. 2(a). For quantum efficiency (QE) measurements monochromatic light was generated either with band pass filters or a monochromator. External QE values were converted to internal QE using the reflectance and absorption spectra of the films. Although the films appear highly resistive at 300 K, elevated temperature thermopower measurements show that they are *n*-type.

The above-band gap PV effect in BFO thin films is illustrated in Fig. 2. (1) The effect is found only when the current flow is perpendicular to the aligned domain walls, Fig. 2(a). For current flow parallel to the domain walls, only photoconductivity is observed [12]. (2) The open-circuit voltage, $V_{OC}$, is linear in the contact spacing $L$, i.e., the number of domain walls traversed by the current, and can be very large: for $L = 200$ $\mu$m, a $V_{OC}$ of 16 V was observed, Fig. 2(b). For an average domain wall spacing of 140 nm the voltage per wall under saturation illumination conditions is ~14 mV. (3) The current, which flows *opposite* to the net polarization, is linear in the light intensity, Fig. 2(c). (4) The open-circuit voltage rises initially linearly with increasing illumination intensity and saturates at high illumination intensity. (5) The overall internal quantum efficiency has a clear onset at the BFO band gap, 2.7 eV, Fig. 2(d), distinguishing the present effect from effects attributed to impurity atoms, as these produce a PV response for below band gap light [6]. The photocurrent is insensitive to the polarization of the incident light.

As we have accurate measurements of the periodic domain structure, it is possible to develop a microscopic

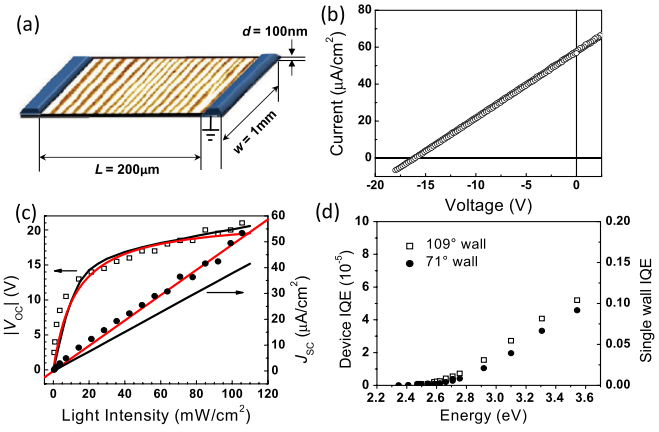


FIG. 2 (color online). (a) Schematic of ferroelectric BFO film with top Pt electrical contacts such that current flow traverses the domain walls. (b) Measured *J*-*V* characteristics under white light illumination (200 mW cm$^{-2}$) showing above-band gap open-circuit voltages for the device shown in (a), (c) Measured $V_{OC}$ and $J_{SC}$ for 375 nm illumination. The black solid lines are the calculated results using the numerical model and the red solid lines are fits to the analytical model (see text). (d) Measured internal quantum efficiency (IQE) for the device (also for 109° wall device) and for a single domain wall (see text).

1D model of the PV effect to discern its origin. For the film whose *J*-*V* data are shown in Fig. 2(b), the domain spacing $d_D$ and the domain wall width $d_{DW}$ are 140 nm and 2 nm, respectively [13]. *Ab initio* calculations and scanning tunneling spectroscopy have suggested that the potential step at the wall, $\Delta\Phi_{DW}$, is of the order of 10's of mV and the band gap in the wall is lowered by about 20% (mainly lowering of the conduction band) [14,15].

We calculated the current density by numerically solving the coupled Poisson's equation and current continuity equations in 1D. Shockley-Read-Hall (SRH) recombination was assumed for nonequilibrium electrons and holes which recombine via midgap traps. Ohmic contact conditions were assumed at the ends of the device for the majority carriers (electrons). A finite difference method with nonuniform meshing was used to solve the problem self-consistently. The periodic electrostatic potential steps are introduced with a ferroelectric polarization discontinuity $\Delta P$ where $P$ is the net domain FE polarization, 53 $\mu$C cm$^{-2}$ [16]. A $\Delta P = 0.08$ $P$ produces a potential step of ~80 mV for a wall width of 2 nm, using a static dielectric constant for BFO of 109.5 $\varepsilon_0$. We assigned the band gap reduction in walls, $\Delta E_{g,DW}$, to the conduction band edge.

In the dark, the electron spatial distribution follows the potential, as expected, Fig. 3(a). Electron and hole concentrations in short-circuit for a carrier generation rate $G$ corresponding to the saturation illumination regime are shown in Fig. 3(b) along with the local recombination rate in Fig. 3(c). Under strong illumination conditions, both electrons and holes are increased in concentration compared to the dark case. The domain wall potential causes electrons and holes to accumulate on opposite sides of the walls, while carriers of the opposite charge are depleted. BFO has a wide gap so that the SRH recombination rate $R$ can be written:

$$R = \frac{np}{\tau_p n + \tau_n p}. \quad (1)$$

For the carrier distributions shown in Fig. 3(b), $R$ has local maxima in the middle of the domains where $n$ and $p$ are similar and also in the domain walls; $R$ decreases significantly near the walls due to depletion of holes on the left side of the wall and electrons on the right. As a result, the regions near the walls act as current sources ($R < G$) as nonequilibrium carriers diffuse against the drift direction toward the center of the domains. One side of the wall produces hole current and the other side produces electron current. In contrast, in the center of the domains, $R > G$ and the hole and electron currents become equal. As shown schematically in Fig. 1(b) this forms the series connections that allows for current continuity and voltage additivity, as in a tandem solar cell. We simulated the evolution of $V_{OC}$ as a function of the number of periods, up to >1000, and found it scales linearly.

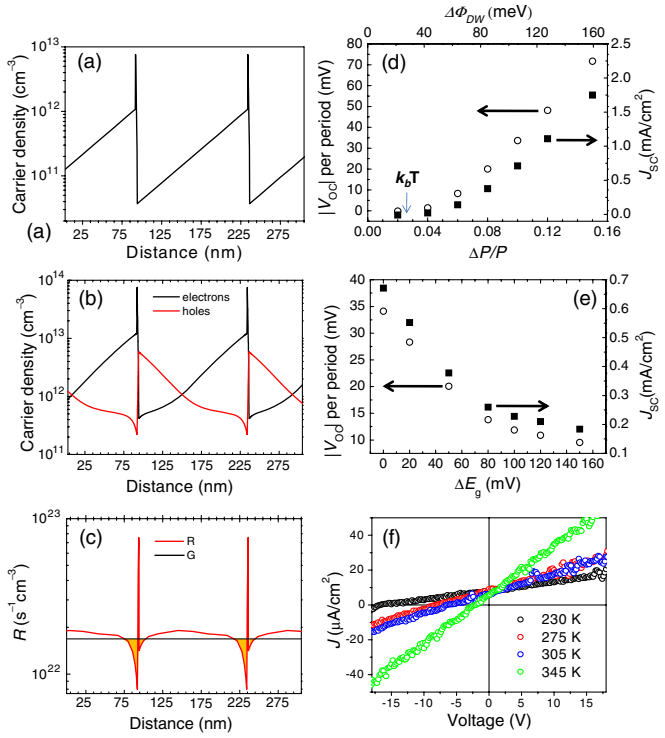


FIG. 3 (color online). (a) Equilibrium carrier concentration of electrons, (b) Short-circuit carrier concentration distribution under illumination for electrons (red) and holes (black), (c) recombination rate $R$ as a function of position across the domain walls. Regions of net current generation ($R < G$) are shaded yellow. (d) Effect of $\Delta P$ on the $V_{oc}$ per wall (left axis) and $J_{sc}$ (right axis) at fixed $\Delta E_g$ (50 meV). (e) Effect of the domain wall band gap reduction $\Delta E_g$ on $V_{OC}$ and $J_{SC}$ at fixed $\Delta P$ ($0.08P_{\text{domain}}$). (f) Temperature-dependent $J$-$V$ curves under nonsaturating illumination at 325 nm wavelength.

Calculated $V_{oc}$ and $J_{sc}$ as a function of illumination intensity are shown as fits to experimental data in Fig. 2(c). A background electron concentration of $2 \times 10^{11}$ cm$^{-3}$ was assumed. The electron and hole mobilities ($\mu_e$, $\mu_h$) are 0.7 and 0.5 cm$^2$ V$^{-1}$ s$^{-1}$, respectively, and lifetimes ($\sim 35$ ps) yielding carrier diffusion lengths $L_e$ and$L_h$ of $\sim$8 nm were used; these values corresponds well to the wall conductivity feature width in [17]. The carrier densities in the device, even under saturation illumination, are sufficiently low [see Fig. 3(b)] such that the Debye length remains larger than the width of the walls. As a result, carrier distributions do not change with applied voltage and the bands remain rigid, producing linear $J$-$V$ plots in agreement with experimental results. $V_{OC}$ and $J_{SC}$ as a function of 375 nm light intensity are shown in Fig. 2(c) (black curves). $V_{OC}$ steadily increases with light intensity and saturates, yielding a $V_{OC}$ saturation of $\sim$20 mV per domain for a potential step of $\sim$80 mV. Importantly, $J_{SC}$ is positive (i.e., flowing against the domain polarization) and increases linearly with light intensity, both of which agree with experimental data shown in Fig. 2(b) and 2(c).

We also explored the effect of key parameters on the magnitude of the PV effect, Figs. 3(d) and 3(e). Above a threshold value of $\Delta P/P$, which corresponds to a potential step on the order of $k_BT$ at ambient temperature, $V_{OC}$ and $J_{SC}$ increase linearly with the magnitude of the potential step due to the creation of a higher blocking $E$-field in the wall. Conversely, a larger band gap reduction at the walls $\Delta E_{g,\text{DW}}$ leads to smaller $V_{OC}$ and $J_{SC}$ by facilitating accumulation of nonequilibrium electrons and holes in the interior of the wall, where the recombination rate is high.

The essential aspects of the effect can be understood with an analytical model, considering the regions of reduced recombination at the domain walls as current sources. The short-circuit current then is given by

$$j_{SC} = q(L_e + L_h)G\text{IQE}_{\text{DW}}, \tag{2}$$

where $\text{IQE}_{\text{DW}}$ can be considered as the internal quantum efficiency due to a single domain wall. The overall conductivity of the device, $\bar{\sigma}$, which has contributions from dark and light conductivity, can be written as

$$\bar{\sigma} = n_0 q \mu_e + q(\mu_e + \mu_h)\bar{\tau}G, \tag{3}$$

where $\bar{\tau}$ captures the relationship between the excess carrier concentration and the generation rate averaged over the device. As we know from both experiment and the 1D modeling the linear $J$-$V$ characteristics of the effect, namely $j(V) = \bar{\sigma}V/L + j_{SC}$, where $L$ is the device length, we can then solve for the open-circuit voltage:

$$V_{OC} = \frac{(L_e + L_h)G\text{IQE}_{\text{DW}}L}{n_0\mu_e + (\mu_e + \mu_h)\bar{\tau}G}. \tag{4}$$

As shown by the red solid lines in Fig. 2(c), Eqs. (2) and (4) show excellent agreement with the model results using $\text{IQE}_{\text{DW}} = 0.11$ and $\bar{\tau} = 135$ ps. Equation (4) predicts that $V_{OC}$ is a function of the overall conductivity of the device. We confirmed this by temperature-dependent measurements shown in Fig. 3(f). Lowering $T$ from 345 to 230 K, which decreases the dark conductivity $\sigma$, increases the $V_{OC}$ by a factor of $\sim$8. Similarly, two-color experiments using sub-band gap illumination to increase photoconductivity result in a decrease in $V_{OC}$.

The experimental IQE data shown in Fig. 2(d) can be analyzed in terms of the efficiency of a single wall. This is done by first multiplying by the number of domains between the contacts, as the domains add in series, and then by considering only the fractional width $(L_e + L_h)/(d_W + d_{\text{domain}})$ of the actual current generating region. As shown by the right hand y-axis for Fig. 2(d), the quantum efficiency for a single wall approaches 10% for above-band gap light. Finally, we discuss the form of the IQE data, which rises monotonically from a threshold at the optical band gap. This behavior shows that the PV effect is not

weaker near the surface of the BFO due to surface recombination or screening of the FE fields by adsorbates, as this would be expected to produce a decrease in the IQE at higher photon energies. It is also notable that the IQE is similar for both 71° and 109° walls whereas the calculated $\Delta E_g$ is larger for the latter case [14]. We think it likely that the effect is due to an increase in the width of the domain walls near the surface, as has been observed previously for $LiNbO_3$ and $LiTaO_3$ surfaces [18,19]. Wider walls would allow for better charge blocking across the wall, further reducing the recombination rate.

We describe the origin of a new PV mechanism driven by the periodic potential structure formed by FE domains. The effect is due to charge separation at the walls, accumulating electrons (holes) on one side and depleting the other carrier. This locally reduces the recombination rate, so that the walls act as current sources. The IQE for this process within a diffusion length of the walls is on the order of 10%. Although we have found the effect in BFO, it should occur in any system with a similar periodic potential structure.

BFO sample fabrication was supported by the Helios Solar Energy Research Center, which is supported by the Director, Office of Science, Office of Basic Energy Sciences of the U.S. Department of Energy. EQE measurements and analysis were supported by the Laboratory Directed Research and Development Program of Lawrence Berkeley National Laboratory. LBNL operates under U.S. Department of Energy Contract No. DE-AC02-05CH11231. J. S. acknowledges support from the Alexander von Humboldt Foundation. D. F. acknowledges support of the Graduate Student Research Innovation Project of the Jiangsu Province of China (Grant No. CX09B_009Z). E. A. L. acknowledges support from Marie Curie Actions under the EMM3 project.

*Corresponding author
JWAger@lbl.gov

[1] S.-Y. Yang *et al.*, Nature Nanotech. **5**, 143 (2010).
[2] P. Würfel, *Physics of Solar Cells* (Wiley, Weinheim, 2009).
[3] J. I. Pankove, Phys. Status Solidi A **61**, 127 (1980).
[4] V. M. Fridkin and B. N. Popov, Phys. Status Solidi A **46**, 729 (1978).
[5] B. I. Sturman and V. M. Fridkin, *The Photovoltaic and Photorefractive Effect in Noncentrosymmetric Materials* (Gordon and Breach, Philadelphia, 1992).
[6] A. M. Glass, D. von der Linde, and T. J. Negran, Appl. Phys. Lett. **25**, 233 (1974).
[7] V. M. Fridkin and B. N. Popov, Sov. Phys. Usp. **21**, 981 (1978).
[8] P. Brody and F. Crowne, J. Electron. Mater. **4**, 955 (1975).
[9] G. F. Neumark, Phys. Rev. **125**, 838 (1962).
[10] S. Y. Yang *et al.*, Appl. Phys. Lett. **95**, 062909 (2009).
[11] Y.-H. Chu *et al.*, Nano Lett. **9**, 1726 (2009).
[12] S. R. Basu *et al.*, Appl. Phys. Lett. **92**, 091905 (2008).
[13] J. Seidel *et al.*, Nature Mater. **8**, 229 (2009).
[14] A. Lubk *et al.*, Phys. Rev. B **80**, 104110 (2009).
[15] Y.-P. Chiu *et al.*, Adv. Mater. **23**, 1530 (2011).
[16] F. Kubel and H. Schmid, Acta Crystallogr. Sect. B **46**, 698 (1990).
[17] J. Seidel *et al.*, Phys. Rev. Lett. **105**, 197603 (2010).
[18] E. A. Eliseev *et al.*, J. Appl. Phys. **106**, 084102 (2009).
[19] A. N. Morozovska *et al.*, Phys. Rev. B **80**, 214110 (2009).